CBPF-NF-064/98

New valleys of cold fission and cluster radioactivity processes from nuclei far from the β-stability line

*O. Rodríguez**, *F. Guzmán**, *S.B. Duarte*, *O. A. P. Tavares*

Centro Brasileiro de Pesquisas Físicas—CBPF/CNPq,
Rua Dr. Xavier Sigaud 150, 22290-180 Rio de Janeiro—RJ, Brazil

*F. García**

Instituto de Física, Universidade de São Paulo,
Caixa Postal 66318, 05315-970 São Paulo—SP, Brazil

M. Gonçalves†

Instituto de Radioproteção e Dosimetria—IRD/CNEN,
Av. Salvador Allende s/n, 22780-160 Rio de Janeiro—RJ, Brazil

ABSTRACT

The present work provides new results for the half-life of cluster radioactivity and cold fission processes from neutron-deficient nuclei of atomic number near proton shell closure. Results are also reported for the half-life of possible decays leading to the neutron-deficient, doubly magic island near ^{100}Sn. The model reproduces the well established experimental systematics of Geiger-Nuttall's diagrams for alpha decay, as well as predicts similar diagrams for heavy cluster emission and cold fission processes.

PACS number(s): 23.70.+j, 24.75.+i, 25.85.Ca

---

*Permanent address: Instituto Superior de Ciências y Tecnologia Nucleares, Av. Salvador Allende y Luaces, Apartado Postal 6163, La Habana, Cuba.

†Electronic address: telo@ird.gov.br.

I. INTRODUCTION

Some aspects of the nuclear structure of neutron-deficient nuclei have been discussed recently using the alpha-decay properties to decide on the persistency of the magicity gap in the structure of proton rich nuclei [1]. A great experimental effort has been devoted in improving the measurement of alpha-decay half-lives of these nuclei in order to get an answer to this problem [2]. These more accurate and recent experimental data can be also used as an exploratory test for the applicability of the theoretical models for cluster emission in the region of nuclei far from the beta-stability line. Also, many astrophysical situations for the development of nucleosynthesis processes in stars need for the knowledge of alpha-radioactivity and fission properties of nuclei far from the beta-stability line [3].

Recently we proposed a model to describe alpha decay and cluster radioactivity processes in a unified theoretical framework [4]. In that model the Coulomb and surface energies for the dinuclear shape were calculated analytically, thus obtaining the barrier penetrability factor for cluster emission and alpha decay. Gamow's penetrability factor [5] was calculated by considering two different inertia coefficients: Werner-Wheeler's coefficient [6] and the effective inertia coefficient [4]. Results have shown a strong dependence of the half-life values on these inertia parameters.

During the last eight years or so, nuclear cold fission and cluster radioactivity processes have been explored intensively both from the experimental and theoretical points of view [7–13]. The occurrence of these processes, for which no neutron-emission takes place, and the total kinetic energy of final fragments practically exhausts the Q-value, is related to shell effects on the barrier penetrability factor. In recent years, new cases of cold fission process have been detected experimentally for ^{230}Th [14], ^{240,242}Pu [14], ^{248}Cm [8], and ^{252}Cf [15] nuclei. In view of these recent detections of the cold fission phenomenon new theoretical approaches have been proposed [9–11] in order to describe the alpha decay, cluster emission and cold fission reactions in a unified image.

The extension of our model to include cold fission calculation and to discuss the role

of the inertia coefficients concerning the half-lives and product yields has been performed [16]. Results have shown a strong dependence of these quantities on the prescription employed in describing the changing of mass asymmetry parameter during the fragmentation process. In addition, we have shown recently on the importance of the inner potential barrier in the calculation of the penetrability factor for cold fission process [17]. In contrast with the expectation by Stefanescu *et al.* [9], the inner part of the potential barrier corresponds to the most significant contribution for the penetrability factor when one deals with heavy cluster emission and cold fission processes [17].

Since our model [4,16] has shown well successful in describing these spontaneous processes near the beta-stability line, we decided to explore the applicability of the model when trying to reproduce results for cluster emission and cold fission processes of very neutron-deficient isotopes. At the same time, we have in mind the great interest which has been devoted in discussing the appearance of the doubly-magic, stable valley in the neutron-deficient region of the tin isotopic family around $^{100}Sn_{50}$, which region can be reached by the cluster radioactivity of some neutron-deficient barium isotopes [4,18,19]. This fact has stimulated researchers to intense experimental and theoretical efforts who have focused their attention on the investigation of different heavy-ion reactions for the formation of neutron-deficient barium nuclei. From theoretical studies the half-life of the process $^{114}Ba \rightarrow {}^{12}C + {}^{102}Sn$ has been calculated in different ways, giving $\tau_{1/2} \sim 10^{10}$ s [19,20]. However, a very recent experiment [21] has indicated a lower limit-value for the half-life of ^{12}C decay from ^{114}Ba as being about six orders of magnitude lower than the calculated results [21]. We recall that, two years ago, we pointed out that the experimental result [18] was not compatible with the prediction from our model for the half-life of ^{12}C decay from ^{114}Ba.

A fundamental ingredient for the correct determination of the half-life of these cluster radioactive processes is the mass-value of the parent, daughter and emitted nuclei. Indeed, it has been already pointed out that a difference of 1 MeV on the Q-value for decay results

in a change up to 5 orders of magnitude for the half-life [17,22,23].

Recent investigations on cluster radioactivity phenomenon have shown that, besides the doubly-magic tin nuclei ($^{100}Sn_{50}$ and $^{132}Sn_{82}$), other nuclei such as some xenon and tellurium isotopes [19] are even possible to be resulting from exotic decays of neutron-deficient barium and cesium isotopes.

The purpose of the present work is to explore the applicability of our model to the region of neutron-deficient nuclei, presenting values for the half-life of cluster emission and cold fission processes leading to doubly-magic, proton-rich, new valleys around $^{100}Sn_{50}$. We point out that our model is able to reproduce the systematic behavior for the half-lives of cold fission processes similar to what is observed in Geiger-Nuttall's diagram for heavy cluster and alpha emission modes.

In Section II we briefly review the fundamentals of our model. The results of half-lives for some cluster radioactivity and cold fission processes for neutron-deficient nuclei are shown in Section III. We also discuss in this Section the prediction for the decay leading to the $^{100}Sn_{50}$ valley. Section IV is devoted to the final and concluding remarks.

II. MODEL DESCRIPTION

The geometric shape parametrization during the pre-scission phase of the fissioning nuclear system is the same adopted in our previous works [4,24]. The dinuclear phase is described in terms of two intersecting spheres, for which configuration the Coulomb potential is well known [25]. We characterize two distinct phases of the separation process: the pre-scission phase, where the fragments are overlapping; and the post-scission phase, where the final fragments are completely defined. For the pre-scission phase two descriptions of mass transfer between the spherical fragments are considered, namely, the Varying Mass Asymmetry Shape (VMAS) and the Constant Mass Asymmetry Shape (CMAS). These two descriptions have been already detailed in Refs. [16,26,27]. In the first description the masses of the nascent fragments, m_1 and m_2, change during the

separation process. The mass asymmetry parameter, $\eta = (m_1 - m_2)\,/\,(m_1 + m_2)$, varies from unit to the final mass asymmetry of the products. The second description imposes that there is no net flux of mass between the spherical fragments, and the value of mass asymmetry is given in terms of the final masses of the nascent products (M_1 and M_2), i.e., $\eta_{\rm F} = (M_1 - M_2)\,/\,(M_1 + M_2)$. In both cases, the configuration of the spherical fragments is determined by the specification of four independent collective coordinates: the radii R_1 and R_2 of the spherical fragments, the distance between the centers of the fragments, ζ, and the distance from the center of heavier nucleus to the intersecting plane of the spherical fragments, ξ, as illustrated in Fig. 1.

To calculate Gamow's penetrability factor [5] for the one-dimensional problem, three of these collective coordinates should be eliminated. By preserving the constraint relationship for the incompressibility of the nuclear matter, we impose that the whole volume of the dinuclear system be constant, i.e.,

$$2(R_1^3 + R_2^3) + 3\left[R_1^2(\zeta - \xi) + R_2^2\xi\right] - \left[(\zeta - \xi)^3 + \xi^3\right] - 4R_0^3 \;=\; 0 \quad , \tag{1}$$

being R_0 the radius of the parent nucleus.

In order to keep the circular shape for the neck connecting the nascent fragments, the following geometric relationship is introduced

$$R_1^2 - R_2^2 - (\zeta - \xi)^2 + \xi^2 \;=\; 0 \quad . \tag{2}$$

Finally, an additional constraint relationship will distinguish the two different descriptions (VMAS or CMAS). To characterize the VMAS description we have considered the radius of the lighter fragment as constant, i.e.,

$$R_1 - \bar{R}_1 \;=\; 0 \, . \tag{3}$$

where $\bar{R}_1$ is the final radius of the light fragment.

In the CMAS description the volume of each fragment is constant, and in terms of the lighter fragment the volume conservation is given by

$$2R_1^3 + 3R_1^2(\zeta - \xi) - (\zeta - \xi)^3 - 4\bar{R}_1^3 \;=\; 0 \quad . \tag{4}$$

Once the system is reduced to the one-dimensional case, the barrier penetrability factor can be calculated in terms of the geometric separation between the centers of the fragments, ζ, by

$$\mathcal{P} \;=\; \exp\left\{-\frac{2}{\hbar}\int_{\zeta_0}^{\zeta_C}\sqrt{2\mu\,(V-Q)}d\zeta\right\} \quad , \tag{5}$$

where ζ_0 and ζ_C are, respectively, the inner and outer turning points, and Q stands for the available total kinetic energy for the final fragments. The total potential energy in this model, V, which appears in Eq. 5, is determined by using an analytical solution of Poisson's equation for the Coulomb part [25], and an effective surface potential of a liquid drop for the nuclear potential. The experimental Q-value is introduced in the calculation to determine the outer turning point $\zeta_C = Z_1 Z_2 e^2/Q$, and also to define the effective surface potential of the drop, by establishing that the difference between the initial and final asymptotic configurations of the fissioning system reproduce the experimental Q-value (see details in Ref. [24]).

The potential barrier is illustrated in Fig. 2 as a function of the ζ coordinate for the three decay modes from ^{234}U parent nucleus. In Fig. 2-(a) we display the result for the alpha-decay process, while in (b) and (c) are displayed the potential barrier for cluster radioactivity and cold spontaneous fission processes, respectively. We remark that no significant difference between the results obtained from the VMAS and CMAS descriptions is observed. Moreover, we have already stressed on the importance of the pre-scission phase for the calculation of Gamow's penetrability factor, since the internal (pre-scission) potential barrier is dominant for the cold fission and cluster radioactivity processes [17]. For alpha decay, on the contrary, the pre-scission phase plays a minor role, but it still accounts to roughly 15% of the total barrier.

As usual, the decay rate is calculated by

$$\lambda \;=\; \lambda_0 \mathcal{P} \quad , \tag{6}$$

where $\lambda_0 = (1.4\text{–}4.8) \times 10^{22}$ s^{-1} is the frequency of assaults on the barrier [27].

To determine Gamow's penetrability factor we need to derive the inertia coefficient, μ, which appears in Eq. 5. The use of Werner-Wheeler's approximation [6] for the velocity field of the nuclear flow to define the inertia tensor coefficient has been largely diffused in the literature [22,24]. In this approach the velocity field is obtained from the solution of the continuity equation and by using the incompressibility and irrotationality constraints for the nuclear flow. After the reduction to the one-dimensional relative motion of the separating parts, only one component of the tensor turns out to be relevant. The expression for Werner-Wheeler's inertia coefficient is given by

$$\frac{1}{2}\int \rho v^2 dr \;=\; \frac{1}{2}\mu_{ww}\dot{\zeta}^{\,2} \quad , \tag{7}$$

with ρ being the mass density for the system, and $\dot{\zeta}$ the relative velocity of the geometric centers of the fragments. Thus, we can determine Werner-Wheeler's inertia coefficients for the two different parametrizations, namely, μ_{ww}^{Vmas} and μ_{ww}^{Cmas}.

An alternative propose for the inertia coefficient has been recently applied in one-dimensional penetrability calculations [4]. By means of a straightforward calculation regarding the constraints above, (Eqs. 1–3), the effective inertia coefficient reads

$$\mu_{\rm eff} \;=\; \mu\alpha^2 \quad , \tag{8}$$

where $\mu = m_1 m_2/(m_1+m_2)$ is the reduced mass of the nascent fragments. The variable α introduces explicitly the dependence of the inertia coefficient on the configuration of the dinuclear system, and it is obtained for the two mass-transfer descriptions defined earlier. For the VMAS description we have,

$$\alpha^{Vmas} \;=\; 1 - \frac{2}{\zeta(R_2-\xi)}\left[(\zeta-\xi)(\bar{z}_1+\bar{z}_2) + \bar{z}_1^{\,2} - \bar{z}_2^{\,2}\right] \quad . \tag{9}$$

The auxiliary variables $\bar{z}_i$ $(i = 1, 2)$ are given by

$$\bar{z}_1 = \frac{\pi}{4}\left[R_1^2 - (\zeta - \xi)^2\right]^2 / v_1 \tag{10}$$

$$\bar{z}_2 = \frac{\pi}{4}\left[R_2^2 - \xi^2\right]^2 / v_2 \ , \tag{11}$$

where $v_1 = \frac{\pi}{3}\left[2R_1^3 + 3R_1^2(\zeta - \xi) - (\zeta - \xi)^3\right]$ and $v_2 = \frac{\pi}{3}\left[2R_2^3 + 3R_2^2\xi - \xi^3\right]$ are the volumes of each spherical fragment.

For the CMAS description, where the volumes of the fragments are constant, we have

$$\alpha^{Cmas} = 1 + \frac{1}{v_1}\left[R_1^2 - (\zeta - \xi)^2\right]\left[R_1 R_1' - (\zeta - \xi)\,(1 - \xi')\right] + \frac{1}{v_2}\left(R_2^2 - \xi^2\right)\left(R_2 R_2' - \xi\xi'\right), \tag{12}$$

with

$$\frac{d\xi}{d\zeta} = \xi' = -\gamma R_2' \ , \tag{13}$$

$$\frac{dR_1}{d\zeta} = R_1' = \frac{1}{R_1}\left[(\zeta - \xi) + (R_2 + \gamma\zeta)\,R_2'\right] \ , \tag{14}$$

$$\frac{dR_2}{d\zeta} = R_2' = -\frac{(\zeta - \xi)\,(6R_1 + 4\zeta - 4\xi) + R_1\,(5R_1 + 3\zeta - 3\xi)}{(R_2 + \gamma\zeta)\,(6R_1 + 4\zeta - 4\xi) + \gamma R_1\,(5R_1 + 3\zeta - 3\xi)} \ , \tag{15}$$

and

$$\gamma = \frac{6R_2 + 4\xi}{5R_2 + 3\xi} \ . \tag{16}$$

The difference between these inertia coefficients has been already shown in Ref. [16]. There we noticed that the effective inertia coefficient in the CMAS description is the most reduced one, in contrast with the largest values obtained with Werner-Wheeler's inertia coefficient calculated in the VMAS description.

III. RESULTS AND DISCUSSION

In the present work we are particularly interested in the study of neutron-deficient nuclei. With the effective liquid drop model above detailed we are now able to investigate

the spontaneous decay of these nuclei by the three different decay modes, namely, alpha decay, cluster radioactivity, and cold fission processes.

A. Alpha emission from neutron-deficient nuclei

The first mode to be analyzed is the alpha decay process. Thus, we display in Fig. 3 the alpha decay half-life-values of parent nuclei of the isotopic families of Rn, Po and Pb. The lines represent our calculated results using the four variants of our model [16,27] (full line represents Werner-Wheeler's inertia coefficient in the VMAS description; the dashed line represents the effective inertia coefficient in the VMAS description; the dotted line is for Werner-Wheeler's inertia coefficient in the CMAS description; and the dot-dashed line represents the effective inertia coefficient in the CMAS description). We can see clearly an excellent agreement between our results and the experimental data (full circles). Note that the remarkable shell effect shown by the data is correctly reproduced by the model in the region of the β-stability line. In addition, good reproducibility is seen even for the cases of very neutron-deficient parent nuclei region.

B. Cluster radioactivity from barium isotopes

An important, recent question related to neutron-deficient nuclei is the formation of a stability valley around the doubly-magic ^{100}Sn nucleus [28–30]. A possible mechanism to reach this valley is by cluster emission from some neutron-deficient Ba isotopes [18,19,21,22,31]. Figure 4 shows the calculated half-lives of possible decays of the Ba isotopic family (mass number in the range $114 \leq A \leq 120$). We present the results showing that Geiger-Nuttall's systematics for different cluster emission is preserved in our model. For barium decay we observe that besides ^{12}C emission, $^{14-16}$O emissions are also possible with experimentally detectable half-lives.

To stress how sensitive are the half-life-values to variation of mass-value of the nuclei

involved in the decay, particularly for the very neutron-deficient isotopes, in Fig. 5 we illustrate the half-life-value of ^{12}C decay from ^{114}Ba as a function of the Q-value for decay. The different lines have the same meaning as in Fig. 3. We note that by using the most recent Mass Table by Audi *et al.* [32] we get $Q = 19.05$ MeV. This Q-value is far from that one corresponding to the experimental lower-limit for the half-life ($Q \approx 22$ MeV). It is important to observe here that the $\mu_{\rm ww}^{Cmas}$ model description is the one which rather approximates to the lower limit for the experimental half-life. Thus, from now on we shall adopt the $\mu_{\rm ww}^{Cmas}$ model description as the current model to deal with the formation of doubly magic tin valleys. In Fig. 5 we also display through the long-dashed line the result by Poenaru *et al.* [22] for carbon radioactivity of Ba. Although the curves have similar behavior, we note that our results deviate by one order of magnitude from Poenaru's results for ^{114}Ba $\rightarrow ^{12}$C $+^{102}$Sn process. The agreement between the models indicates that new experimental efforts should be done to enhance the beam intensity in order to achieve this lower limit for the half-life of the decay process.

C. Cluster radioactivity and cold fission processes leading to tin daughter valleys far from the β-stability line

In Fig. 6. we display by contour lines the most favored decays from parent nuclei of the Mass Table by Audi *et al.* [32] which produce daughter nuclei near ^{100}Sn. Concerning the cluster radioactivity phenomenon, it is observed that ^{12}C nucleus presents the deepest valley of half-life, followed by ^{16}O. The daughter nuclei which corresponds to the lowest half-life-values for cluster radioactivity are ^{102}Sn, ^{103}Sn, and ^{104}Sn. Table I lists the most favorable decays obtained from our model. Figure 6 together with Table I show clearly that there are others possible decay processes in addition to carbon radioactivity from barium leading to tin-daughter nuclei. As a matter of fact, our prediction for $^{13-15}$N, $^{14-16}$O, ^{17}F and ^{20}Ne emissions furnishes experimentally measurable half-lives leading to magic tin daughter nuclei.

In addition, we decided to investigate the cold fission processes leading to ^{100}Sn isotope. In Fig. 7 we display in a contour-plot the half-lives of measurable cold fissioning nuclei leading to neutron-rich, doubly-magic isotopes. It can be seen clearly from Fig. 7 that there are some tin valleys around $^{132}Sn_{82}$ nucleus which are due to the cold fission of several heavy nuclei, asserting that besides the cluster radioactivity phenomenon, the cold fission process also leads to new neutron-deficient or neutron-rich, doubly-magic valleys not explored so far neither from the experimental nor theoretical points of view.

D. Geiger-Nuttall's systematics for cold fission processes

As a final result we display in Figs. 8–10 Geiger-Nuttall's plots for neutron-deficient isotopes of Po, Bi and Pb, respectively. According to Kumar and Gupta [31], the different slopes of Geiger-Nuttall's plot for cluster emission (part-a of Figs. 8–10) are associated with different preformation factors for each emission mode. The remarkable half-life-trends exhibited in Figs. 8–10 point out that our effective liquid drop model gives the same Geiger-Nuttall's systematics for cold fission processes as those observed for alpha and cluster emission (the cold fission systematics is depicted in part-b of Figs. 8–10). The small deviation from linearity observed in a few cases can be explained in terms of the nuclear structure effects, which are not present in the total potential adopted in our model. We call attention to the fact that the points in Figs. 8–10 represent predictions for favored cases of cold fission for Po, Bi, and Pb isotopes not yet investigated from the experimental point of view.

IV. CONCLUSION AND FINAL REMARKS

The decay modes of some neutron-deficient nuclei have been investigated in the present work. We have observed that shell effects, which are implicitly being taken into account in our model through the Q-value for decay, are decisive when calculating the half-lives

of alpha decay, cluster radioactivity, and cold fission processes for these nuclei. Results obtained for the ^{12}C emission from ^{114}Ba nucleus in the framework of our model are compatible with the experimental data [21]. Other processes, such as the emission of ^{16}O from barium isotopes, can also be observed with higher half-life, but still in the experimentally detectable range. Although ^{114}Ba nucleus has been obtained very recently in experiments of heavy-ion reactions, its mass is yet not well established. We have already commented in a previous work that small changes in the Q-value (greater than 0.5 MeV) can change by a few orders of magnitude the decay half-life-value [17]. Thus we expect that further improvements in the production and detection of neutron-deficient nuclei can bring our results for barium decay half-life to closer agreement with these new data.

By means of our routine calculation, we present here new cluster radioactivity valleys which have tin nuclei as the final state of the spontaneous reaction. Regarding the trans-tin radioactivity, the most favored processes are those for which one of the ^{102,103,104}Sn isotopes is the daughter nucleus. These decays characterize new emission valleys around the ^{100}Sn nuclei. This is an evidence for mainly $^{14\text{–}16}$O emissions be also observed experimentally in a near future, since their half-life-values are only five orders of magnitude longer than the measured half-life for ^{12}C emission from ^{114}Ba. However, by the time being, ^{114}Ba production is not sufficiently intense to allow for the detection of ^{16}O emission. We are hopeful that in further experiments the beam intensity and the detection techniques could be improved in such a way that this decay process become experimentally observed.

The conclusions drawn here emerge in the context of the CMAS mass transfer description and Werner-Wheeler's inertia coefficient ($\mu_{\rm ww}^{Cmas}$). Small differences among the various model combinations shown in Fig. 4 indeed exist, but due to the general trend exhibited by the model combinations we can state that all of them lead to similar results and conclusions regarding to the doubly magic tin valleys attained from both cluster radioactivity and cold fission processes of heavy parent nuclei.

In the present work we do not include the deformation of both the parent and daughter nuclei directly in the calculation. This effect is introduced partially in the model through the experimental Q-value for decay, which is also considered when defining the effective potential in the model calculation. In addition, the exact mass-value of the decaying nucleus is a key element to determine precisely the half-life of a given decay. Since we are using mass-values from the Mass Table by Audi *et al.* [32], we expect that the use of new mass-values of nuclei which are being produced in accelerators [29] can improve our results by one or two orders of magnitude. As a final remark, we would like to mention that other effects, such as dissipation during the separation process, should be significative to the calculation of Gamow's penetrability factor. We are working on the inclusion of dissipative degrees of freedom in the present model to investigate the importance of thermal dissipation in the half-life of the decaying nuclei.

Acknowledgment

The authors would like to express their gratitude to the Brazilian CNPq, FAPERJ, and CLAF for partial support.

[1] J. Wauters, P. Dendooven, M. Huyse, G. Reusen, P. Van Duppen, P. Lievens, and the ISOLDE Collaboration, Phys. Rev. C **47**, 1447 (1993); J. Wauters *et al.*, Phys. Rev. C **55**, 1192 (1997); J. C. Batchelder, K. S. Toth, C. R. Bingham, L. T. Brown, L. F. Conticchio, C. N. Davids, D. Seweryniak, J. Wauters, J. L. Wood, and E. F. Zganjar, Phys. Rev. C **55**, R2142 (1997); A. N. Andreyev, N. Bijnens, T. Enqvist, M. Huyse, P. Kuusiniemi, M. Leino, W. H. Trzaska, J. Uusitalo, and P. Van Duppen, Z. Phys. A **358**, 63 (1997).

[2] R. D. Page, P. J. Woods, R. A. Cunningham, T. Davinson, N. J. Davis, A. N. James, K. Livingston, P. J. Sellin, and A. C. Shotter, Phys. Rev. C **53**, 660 (1996); T. Enqvist, K. Eskola, A. Jokinen, M. Leino, W. H. Trzaska, J. Uusitalo, V. Ninov, and P. Armbruster, Z. Phys. A **354**, 1 (1996); M. Leino *et al.*, Z. Phys. A **355**, 157 (1996).

[3] G. Wallerstein *et al.*, Rev. Mod. Phys. **69**, 995 (1997).

[4] S. B. Duarte and M. G. Gonçalves, Phys. Rev. C **53**, 2309 (1996).

[5] G. Gamow, Z. Phys. **51**, 204 (1928).

[6] D. N. Poenaru, J. A. Maruhn, W. Greiner, M. Ivascu, D. Mazilu, and I. Ivascu, Z. Phys. A **333**, 291 (1989).

[7] V. Avrigeanu, A. Florescu, A. Săndulescu and W. Greiner, Phys. Rev. C **52**, R1755 (1995).

[8] A. Benoufella, G. Barreau, M. Asghar, P. Audouard, F. Brisard, T. P. Doan, M. Hussonnois, B. Leroux, J. Trochon, and M. S. Moore, Nucl. Phys. A **565**, 563 (1993).

[9] E. Stefanescu, W. Scheid, A. Sandulescu and W. Greiner, Phys. Rev. C **53**, 3014 (1996).

[10] A. Florescu, A. Sandulescu, C. Cioaca and W. Greiner, J. Phys. G **19**, 669 (1993).

[11] S. Singh, R. K. Gupta, W. Scheid and W. Greiner, J. Phys. G **18**, 1243 (1992).

[12] E. Stefanescu, A. Sandulescu and W. Greiner, J. Phys. G **20**, 811 (1994).

[13] W. Greiner and A. Sandulescu, J. Phys G **17**, S429 (1991).

[14] M. Asghar, N. Boucheneb, G. Medkour, P. Geltenbort, and B. Leroux, Nucl. Phys. A **560**, 677 (1993).

[15] J. H. Hamilton *et al.*, J. Phys. G **20**, L85 (1994); J. H. Hamilton, A. V. Ramayya, S. J. Zhu, G. M. Ter-Akopian, Yu. Ts. Oganessian, J. D. Cole, J. O. Rasmussen, and M. A. Stoyer, Prog. Part. Nucl. Phys. **35**, 635 (1995).

[16] S. B. Duarte, O. Rodríguez, O. A. P. Tavares, M. Gonçalves, F. García, and F. Guzmán, Phys. Rev. C **57**, 2516 (1998).

[17] S. B. Duarte, M. G. Gonçalves, and O. A. P. Tavares, Phys. Rev. C **56**, 3414 (1997).

[18] A. Guglielmetti *et al.*, Phys. Rev. C **52**, 740 (1995).

[19] A. Florescu and A. Insolia, Phys. Rev. C **52**, 726 (1995).

[20] D. N. Poenaru and W. Greiner, J. Phys. G **17**, S443 (1991).

[21] A. Guglielmetti *et al.*, Phys. Rev. C **56**, R2912 (1997).

[22] D. N. Poenaru, W. Greiner and E. Hourani, Phys. Rev. C **51**, 594 (1995).

[23] H. G. de Carvalho, J. B. Martins, and O. A. P. Tavares, Phys. Rev. C **34**, 2261 (1986).

[24] M. Gonçalves and S. B. Duarte, Phys. Rev. C **48**, 2409 (1993).

[25] M. Gaudin, J. Phys. **35**, 885 (1974).

[26] M. Gonçalves, S. B. Duarte, F. García, and O. Rodríguez, Compt. Phys. Commun. **107**, 246 (1997).

[27] O. A. P. Tavares, S. B. Duarte, O. Rodríguez, F. Guzmán, M. Gonçalves, and F. García, J. Phys. G: Nucl. Part. Phys. **24**, 1757 (1998).

[28] R. Schneider *et al.*, Z. Phys. A **348**, 241 (1994).

[29] M. Chartier *et al.*, Phys. Rev. Lett. **77**, 2400 (1996).

[30] Guglielmetti et *al.*, Nucl. Phys. A **583**, 867 (1995).

[31] S. Kumar and R. K. Gupta, Phys. Rev. C **49**, 1922 (1994).

[32] G. Audi, O. Bersillon, J. Blachot, and A. H. Wapstra, Nucl. Phys. A **624**, 1 (1997).

Figure captions:

Fig. 1: Schematic representation of the configuration of the dinuclear decaying system. The daughter nucleus and the emitted (smaller) fragment have radius R_2 and R_1, respectively, and the distance between the geometrical centers of the fragments is denoted by ζ. The variable ξ represents the distance between the center of the heavier fragment and the circular sharp neck of radius a.

Fig. 2: Potential barrier for three decay modes of ^{234}U parent nucleus. a) shows the internal part of the potential (shaded area) for the alpha decay process; the same is shown for ^{28}Mg cluster emission (b), and the cold fission mode $^{234}\mathrm{U} \rightarrow {}^{100}\mathrm{Zr} + {}^{134}\mathrm{Te}$ (c). The horizontal dashed line represents the Q-value in each case. It is not possible to observe from the figure differences between the curves when calculated with the VMAS and CMAS descriptions. The importance of the inner (pre-scission) part of the potential is clearly shown.

Fig. 3: Alpha decay half-life for Rn (a), Po (b), and Pb (c) proton-rich isotopes. It is seen clearly a pretty good agreement with the experimental data (full circles). The full-, dashed-, dotted- and dot-dashed-lines (most of them coincides) represent, respectively, the μ_{ww}^{Vmas}, $\mu_{\mathrm{eff}}^{Vmas}$, μ_{ww}^{Cmas}, and $\mu_{\mathrm{eff}}^{Cmas}$model combination. The figure asserts that the present model is a good tool to provide new alpha-decay half-life predictions for nuclei far from the β-stability line.

Fig. 4: Geiger-Nuttall's plot for barium parent isotopes ($Z = 56$, $A = 114$–120). The steep sequences of points represent different families of emitted nuclei (^{12}C, and $^{14\text{–}16}$O as indicated). Parts (a), (b), (c), and (d) refer, respectively, to μ_{ww}^{Vmas}, $\mu_{\mathrm{eff}}^{Vmas}$, μ_{ww}^{Cmas}, and $\mu_{\mathrm{eff}}^{Cmas}$.

Fig. 5: Half-life of $^{114}\mathrm{Ba} \rightarrow {}^{12}\mathrm{C} + {}^{102}\mathrm{Sn}$ process as a function of Q-value for decay. Lines represent different model combinations as indicated. The long-dashed line represents the results by Poenaru *et al.* [22]. The experimental lower-limit quoted in Ref. [21] is $\tau_{\mathrm{e}} \geq 10^4$s (horizontal thin line).

Fig. 6: Valleys of cluster radioactivity with daughter tin nuclei following the $\mu_{\rm ww}^{Cmas}$ model combination. It is noted the deeper cluster radioactivity valleys for ^{12}C and $^{14-16}$O emissions. These results can be used as insight to further experiments.

Fig. 7: Valleys of cold fission processes with daughter tin nuclei. The model combination used is the $\mu_{\rm ww}^{Cmas}$.

Fig. 8: Geiger-Nuttall's plot for cluster radioactivity (part-a) and cold fission (part-b) processes of polonium neutron-deficient isotopes. Each isotopic family is displayed by different symbols as indicated (only for part-b of this figure the symbols are: open diamonds, Sr; crosses, Y; and open triangle, Mo). The thin lines are drawn only to guide the eyes.

Fig. 9: The same as in Fig. 8, but for bismuth isotopes.

Fig. 10: The same as in Fig. 8, but for lead isotopes.

Table I: Calculated half-life ($\log_{10}\tau$ (s)) for the most probable decays of intermediate-mass parent nuclei producing tin isotopes. The present half-life-values have been obtained by using Werner-Wheeler's inertia coefficient in the CMAS description, μ_{ww}^{Cmas} (note that alpha decay results are also shown in the table).

Product	$\log_{10}\tau$ (s) for various cluster emissions								
Nucleus	^{4}He	^{12}C	^{13}N	^{14}N	^{15}N	^{14}O	^{15}O	^{16}O	^{17}F
^{102}Sn	-4.02	9.76	—	—	27.31	—	—	—	—
^{103}Sn	-2.71	11.68	—	27.76	—	—	—	14.06	—
^{104}Sn	0.51	14.32	19.80	23.18	—	—	19.57	16.30	23.70
^{105}Sn	1.97	17.02	24.25	—	—	27.44	—	18.66	—
^{106}Sn	5.99	19.63	27.45	—	—	—	26.12	21.12	—
^{107}Sn	6.62	23.40	—	—	—	—	—	24.14	—
^{108}Sn	10.20	—	—	—	—	—	—	27.46	—
^{109}Sn	15.85	—	—	—	—	—	—	—	—
^{110}Sn	23.68	—	—	—	—	—	—	—	—

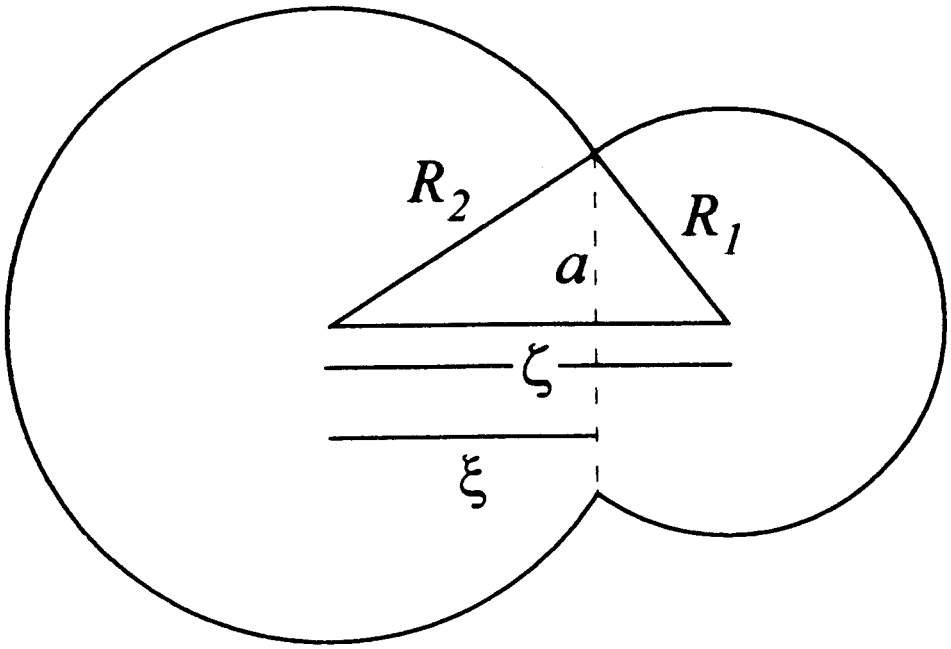

Fig. 1
Rodriguez et al.

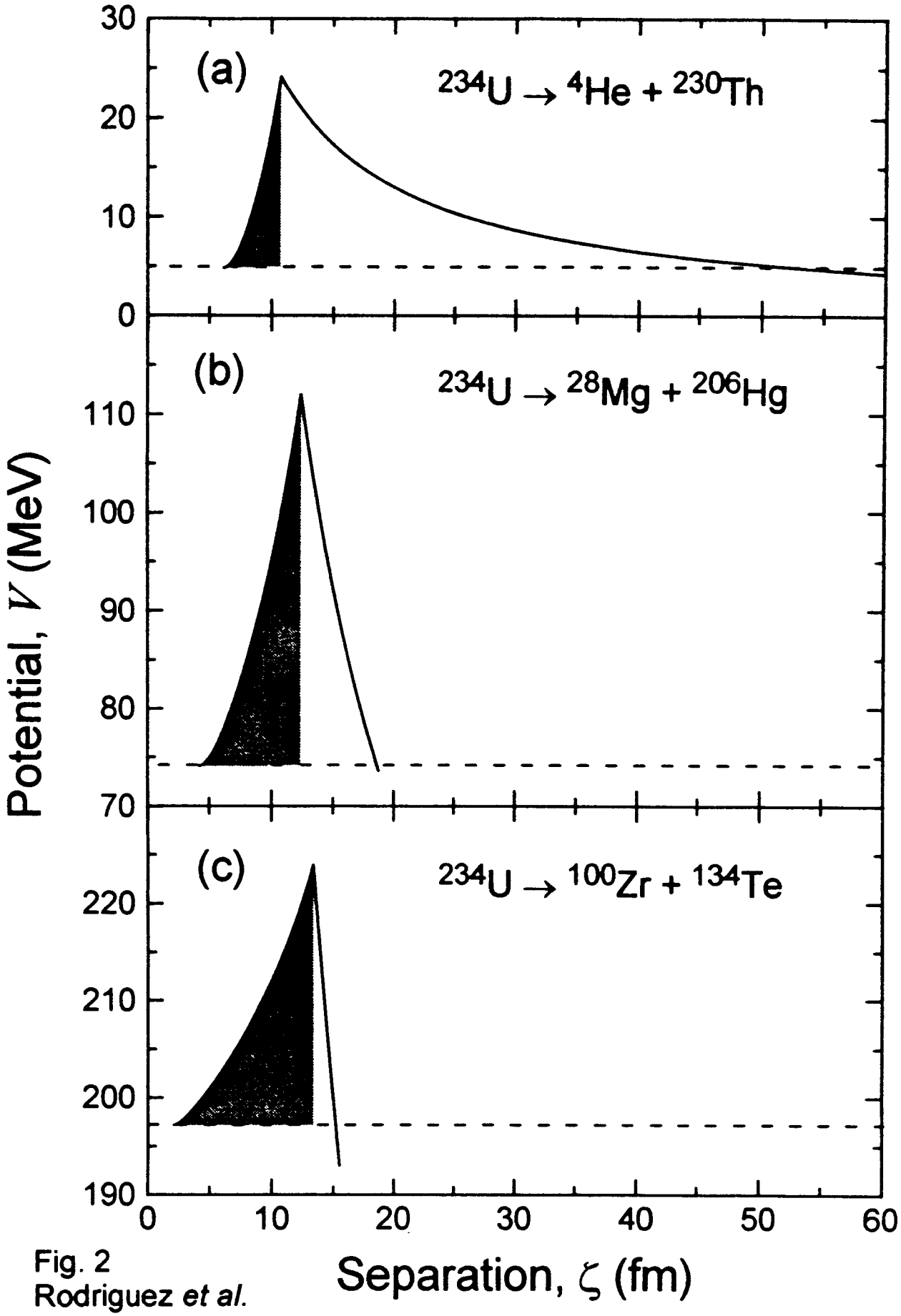

Fig. 2
Rodriguez *et al.*

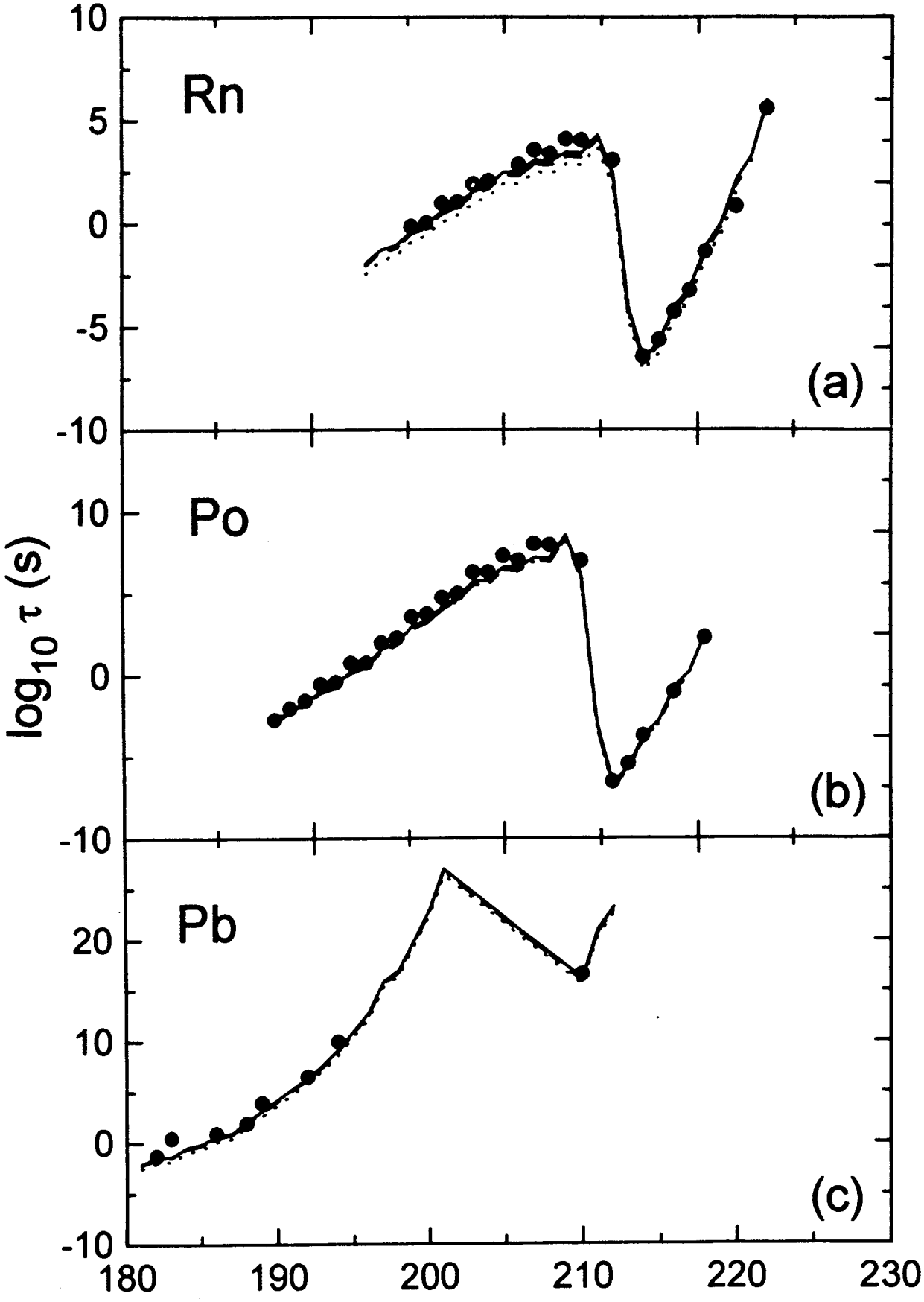

Fig. 3
Rodriguez et al.

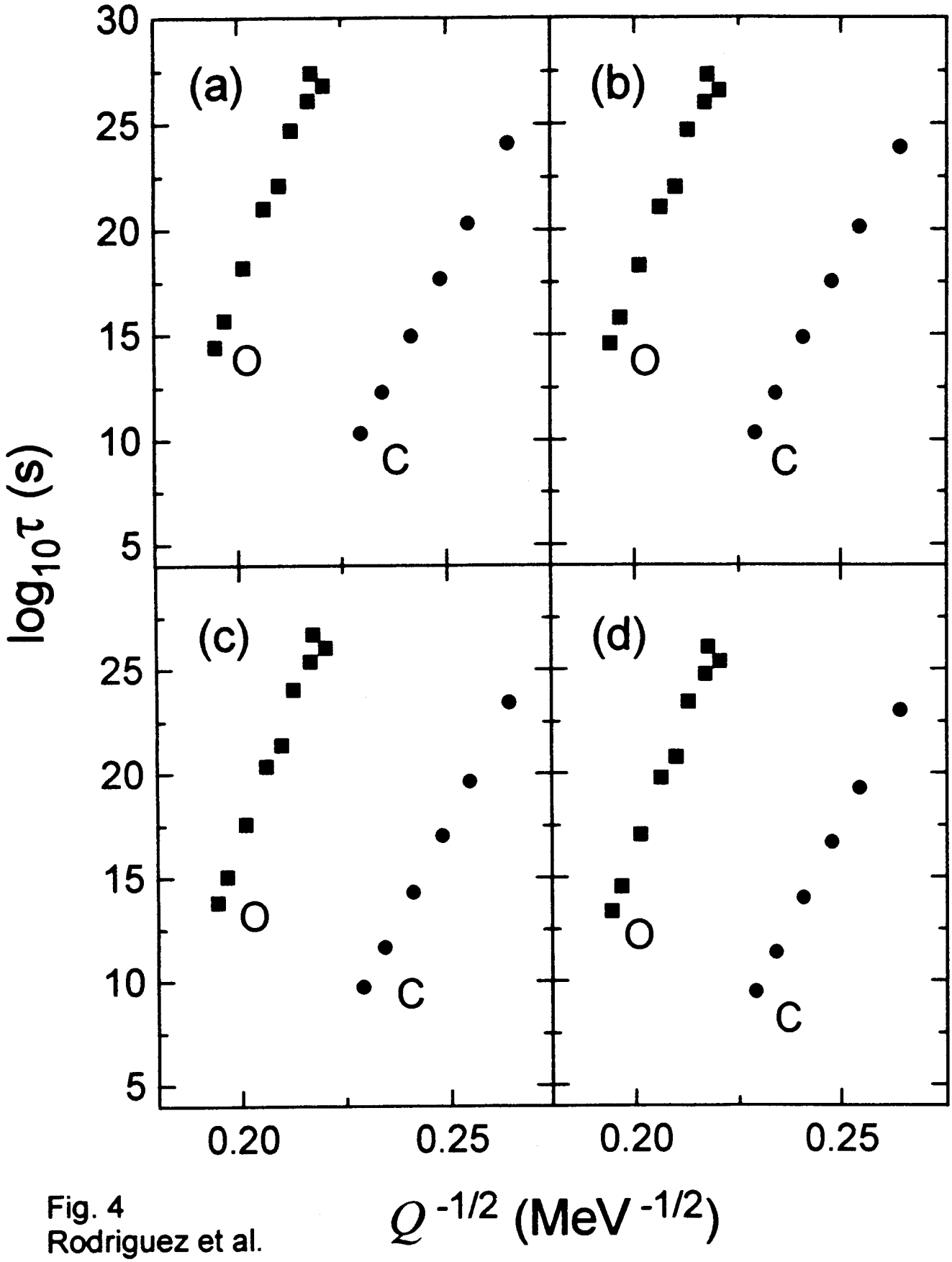

Fig. 4
Rodriguez et al.

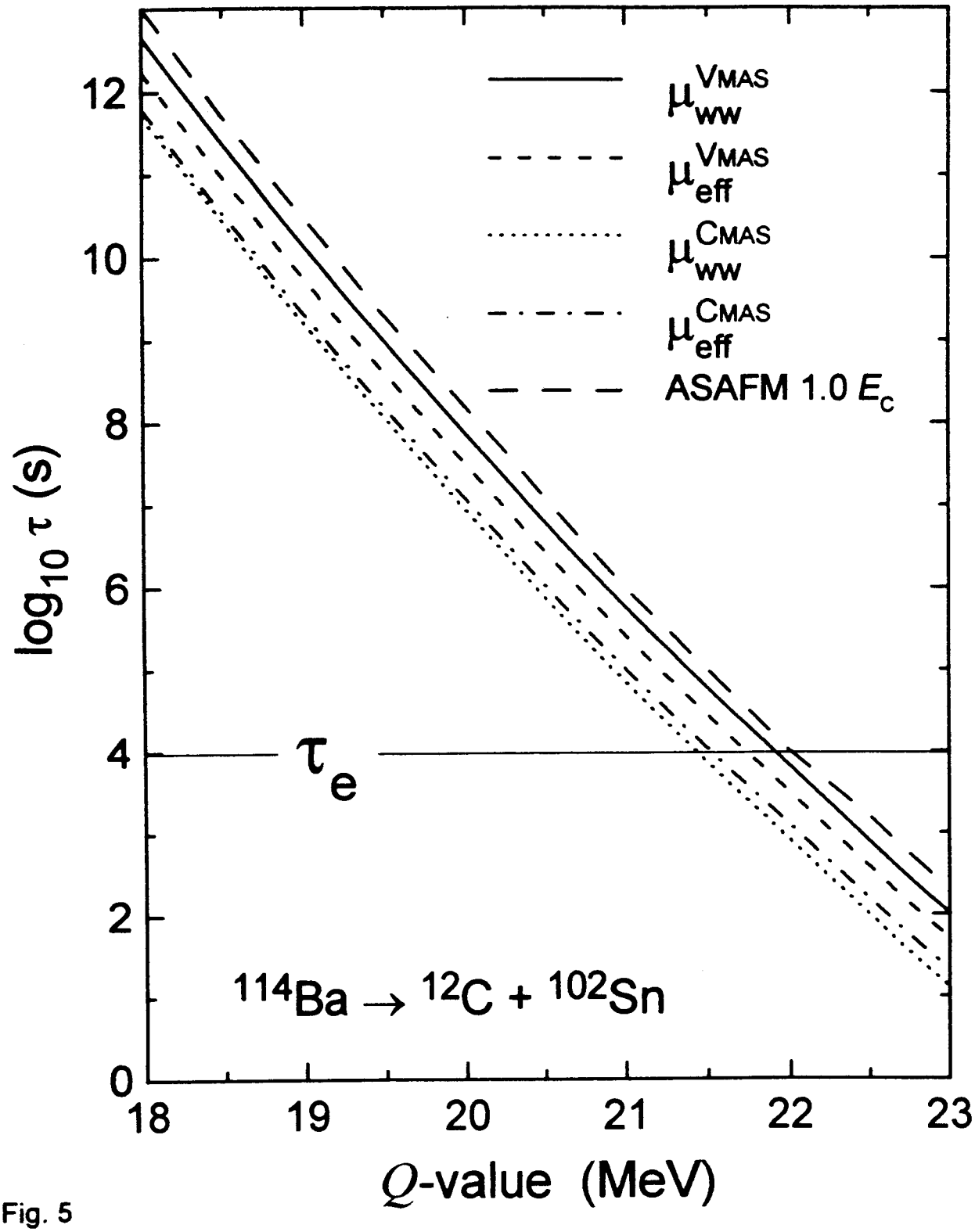

Fig. 5
Rodriguez *et al.*

Fig. 6
Rodriguez *et al.*

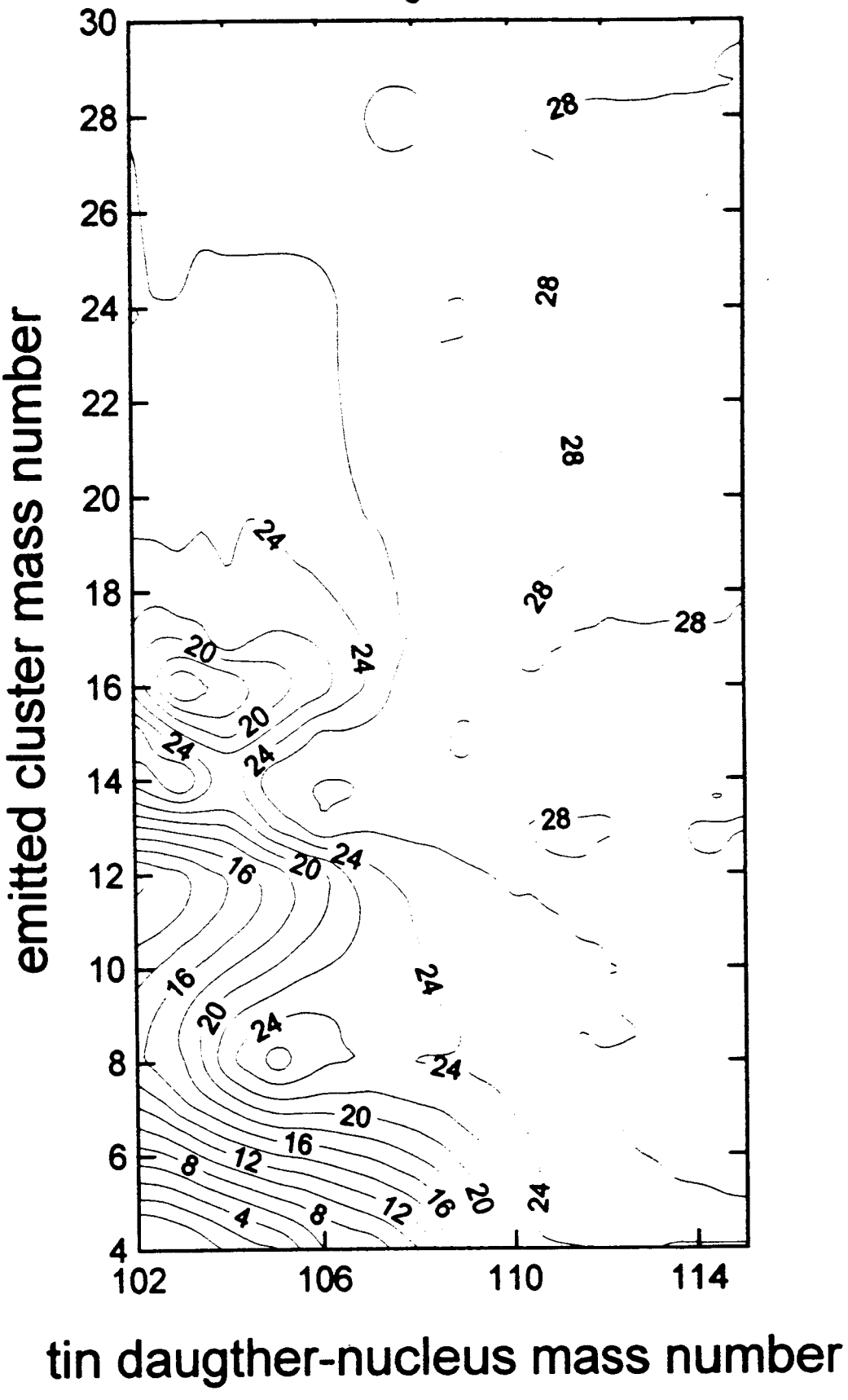

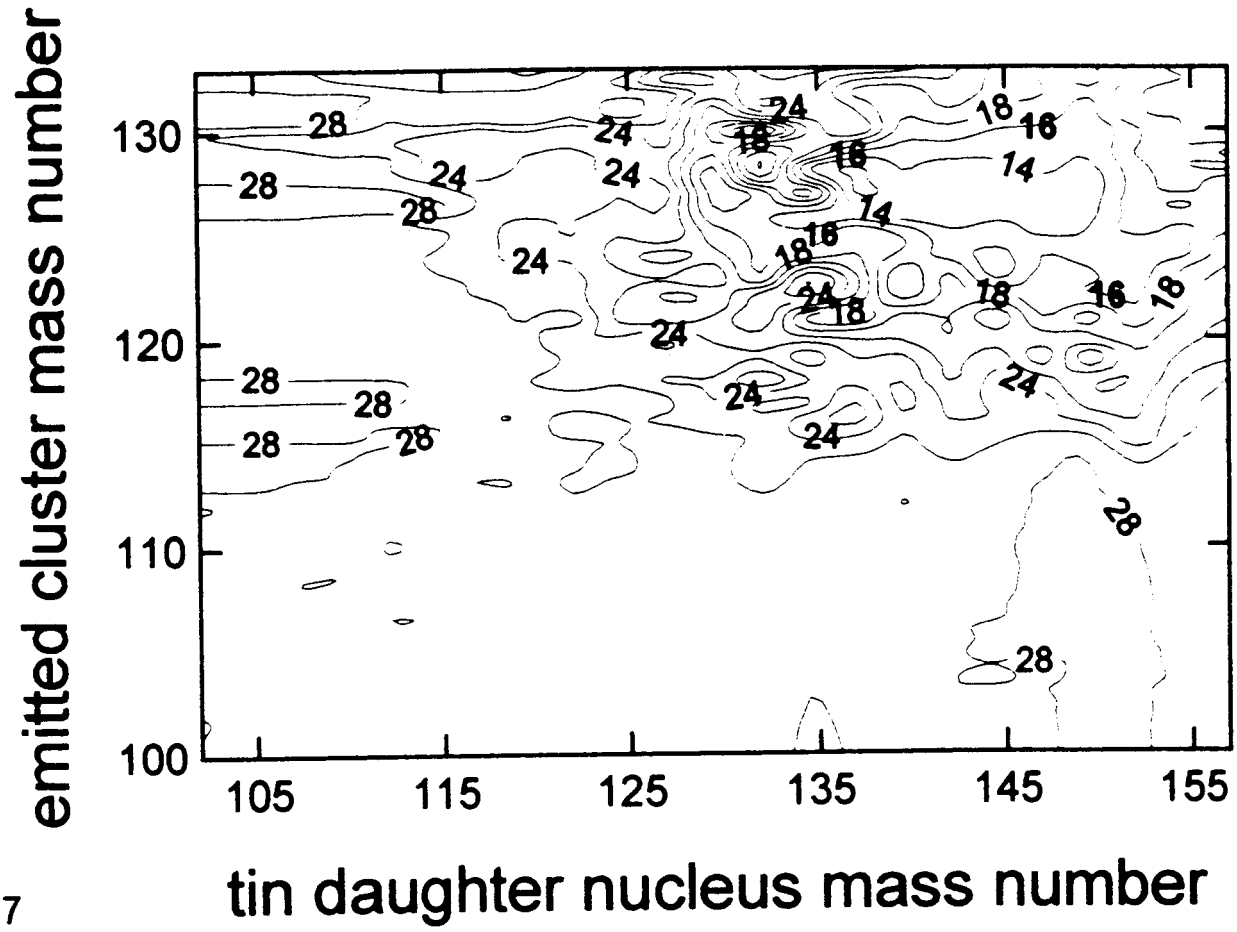

Fig.7
Rodriguez *et al.*

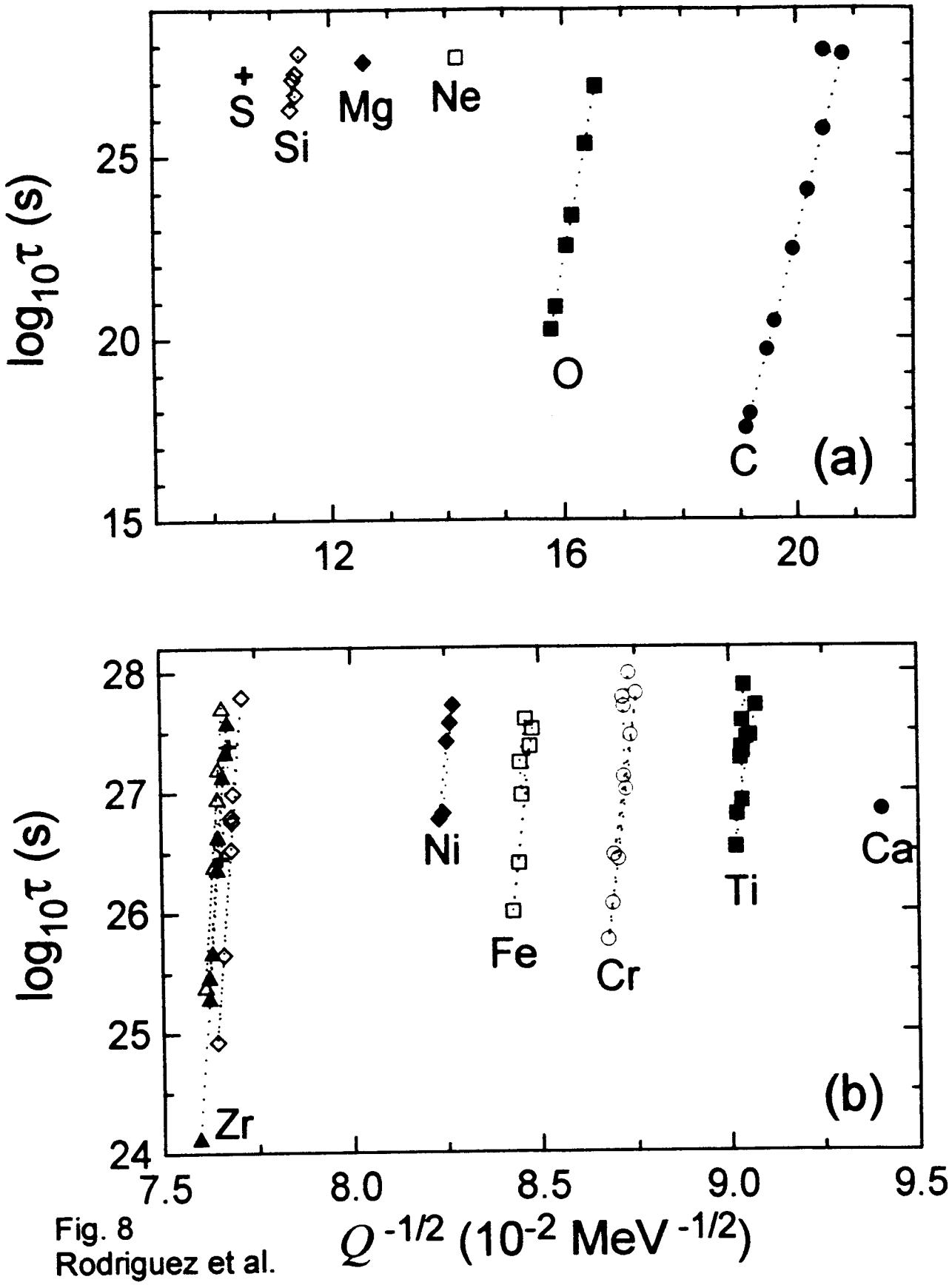

Fig. 8
Rodriguez et al.

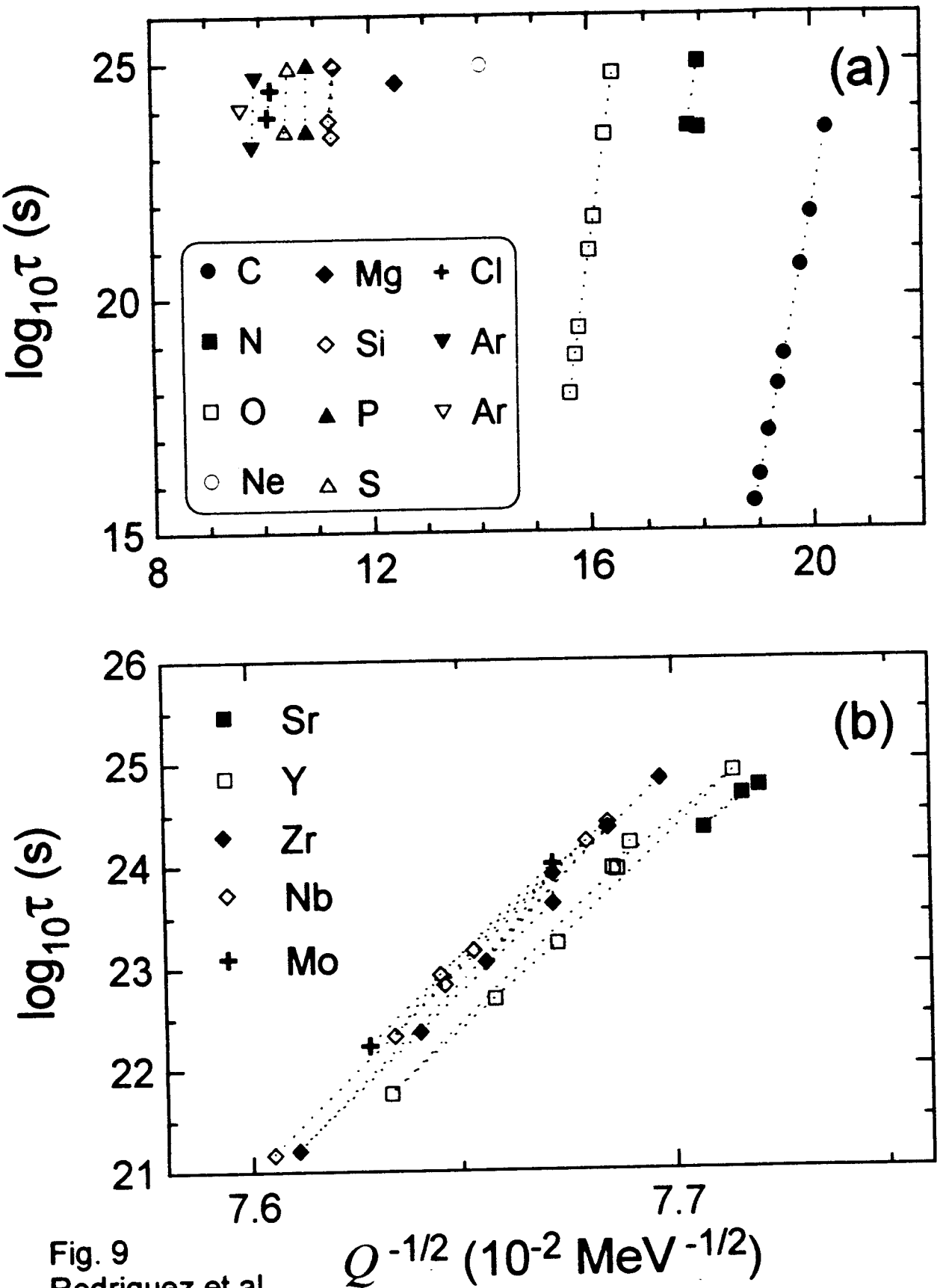

Fig. 9
Rodriguez et al.

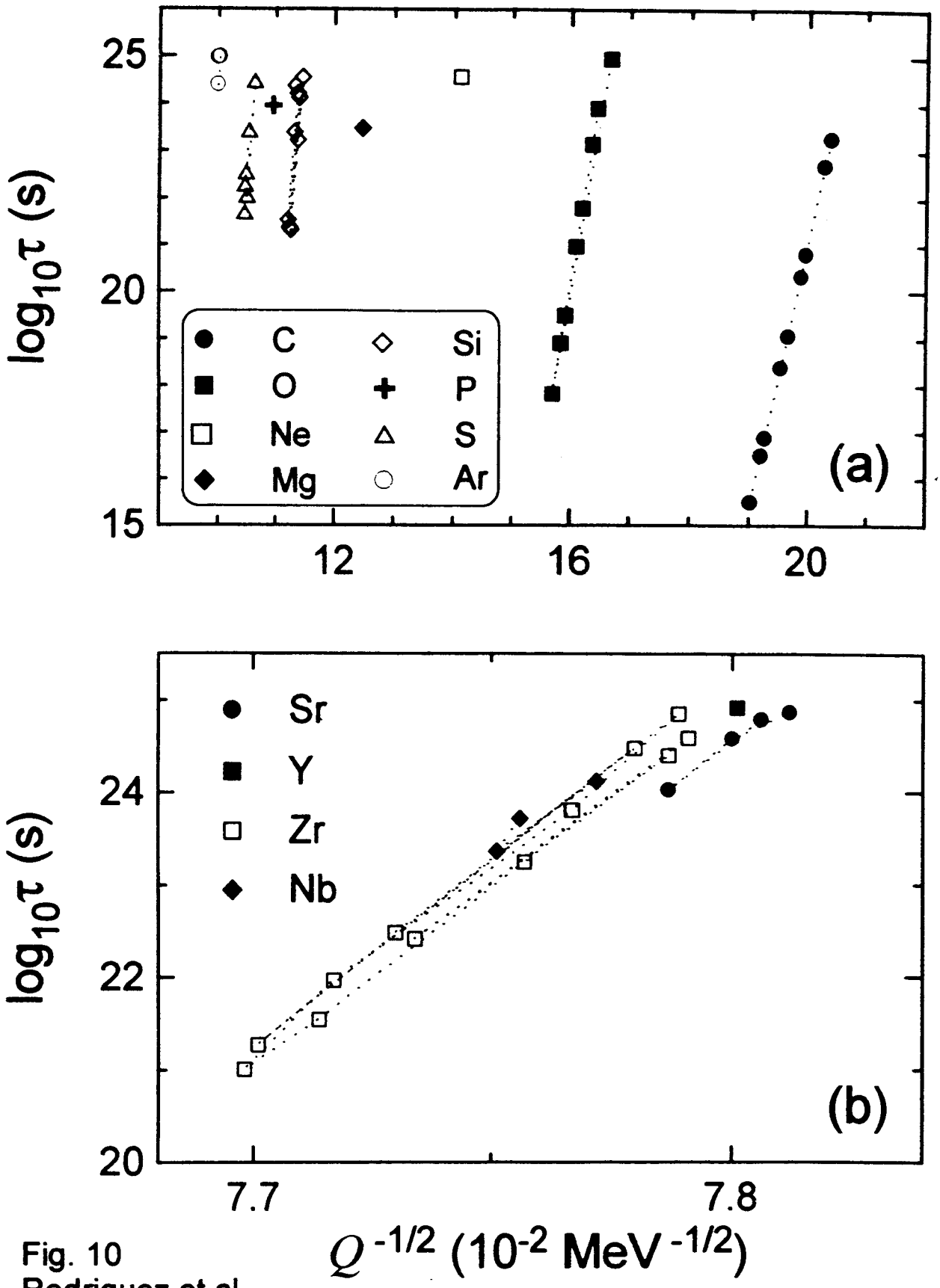

Fig. 10
Rodriguez et al.